Estimation of the L-, M-, and S-cone weights of the postreceptoral detection mechanisms

Marcel J. Sankeralli and Kathy T. Mullen

McGill Vision Research, Department of Ophthalmology, McGill University, H4-14, 687 Pine Avenue West, Montreal, Quebec H3A 1A1 Canada

Received June 22, 1995; accepted November 28, 1995; revised manuscript received November 30, 1995

We have obtained two- and three-dimensional detection threshold contours in cone contrast space for sinusoidal gratings for three subjects at three spatiotemporal conditions (1 cycle/degree (c/deg), 0 Hz; 0.125 c/deg, 0 Hz; 1 c/deg, 24 Hz). These conditions were chosen to favor the response of each of the three postreceptoral mechanisms in turn. Contours were obtained from measurements in as many as 60 axes in (L, M, S) cone contrast space and were fitted by superellipses. Our technique permitted us to improve on earlier estimates of the cone weightings to the mechanisms. We found that the red–green mechanism has an input cone weighting of L−M with a 2% S-cone input; the luminance mechanism has a weighting of kL + M, where k varies between 3 and 5 at the high-temporal condition, with a 5% S-cone input in opposition to L- and M-cones; and the blue–yellow mechanism consists of S inputs in closely balanced opposition to L and M inputs. These cone weights were found to be consistent among our three subjects.

1. INTRODUCTION

Psychophysical studies have consistently revealed three postreceptoral detection mechanisms in humans: a red–green mechanism having opponent L- and M-cone inputs (pL − qM),[1,2] a blue–yellow mechanism involving S-cones in opposition to L and M cones (pS − qL − rM),[3] and a luminance mechanism with additive L- and M-cone inputs with at best a weak input from S cones [pL + qM(+rS)].[4–6] Measurements of detection threshold contours in cone contrast space have provided estimates of the cone weightings to these mechanisms.[7–12] These methods have shown that the red–green mechanism consists of L and M inputs in exact opposition but have been less conclusive about cone weightings to the luminance and blue–yellow mechanisms.

Our study adds to earlier methods of measuring threshold contours[7–12] in the following respects. First, we measure contours at three spatiotemporal conditions. This allows us to reveal selectively the threshold contours of the three color and luminance mechanisms in turn. Second, we supply a fit (the superellipse) having a shape parameter in addition to those of the ellipse. This has enabled us to obtain better fits and, as we will show, more-precise estimates than earlier studies that used elliptical contours.[7,8,13–15] Third, in addition to obtaining two-dimensional contours, we determine three-dimensional threshold contours from measurements along evenly spaced axes. This extends previous analysis[9,12] to include S-cone inputs and yields a more uniform sampling of color space than did previous studies.[11]

2. METHODS

A. Stimuli and Apparatus

We measured detection threshold contours at three spatiotemporal conditions: (1) 1.0 cycle/degree (c/deg), 0 Hz—termed the mid-spatial, low-temporal (Gaussian temporal envelope only) condition; (2) 0.125 c/deg, 0 Hz—the low-spatial, low-temporal condition; and (3) 1.0 c/deg, 24 Hz—the mid-spatial, high-temporal condition. The two low-temporal conditions were used to investigate the red–green and blue–yellow mechanisms, respectively,[16–20] and the high-temporal condition was used to investigate the luminance mechanism.[21,22] Spatial frequencies not exceeding 1 c/deg were used to minimize luminance artifacts that were due to chromatic aberration.[23,24] The stimuli were viewed at 150 cm for the mid-spatial conditions and at 50 cm for the low-spatial condition. The screen subtended an angle of 12° at 150 cm and 35° at 50 cm. The phosphor CIE chromaticities were (0.64, 0.34), (0.28, 0.60), and (0.15, 0.06), respectively.

We used sinusoidal spatially and temporally varying Gaussian enveloped gratings presented upon a white background with a 4′ black fixation spot. The gratings were created by the superposition in phase of gratings produced by the three phosphors, each having an irradiance profile of the form

$$I = I_0[1 + C\ \exp(-y^2/2{\sigma_y}^2)\sin\ 2\pi f_y y \times \exp(-t^2/2{\sigma_t}^2)\sin\ 2\pi f_t t], \quad (1)$$

where I is the irradiance of a given phosphor, I_0 is the fixed phosphor background irradiance, and C is the phosphor contrast. The spatial standard deviation σ_y was 1.4 cycles in all three spatiotemporal conditions. The temporal standard deviation σ_t was fixed at 88 ms. The grating was also hard-edge windowed in a vertical strip of width $2\sigma_y$: the region outside the window was at the background condition.

The stimuli were presented on a Barco CCID 7651 RGB color monitor driven by a Cambridge Research Systems VSG2/1 video controller interfaced with a Dell 333D computer. The monitor had a pixel resolution of 672 × 750, with a frame rate of 75 Hz and a line rate of 60 kHz. The background was set at 54 cd m^{-2} near the equal-energy white point [Judd (0.28, 0.30)].

0740-3232/96/050906-10$10.00

Each video output was driven by a 14-bit digital-to-analog converter fed from a 12-to-14-bit lookup table (LUT). The LUT's were used to linearize the relationship between the LUT digital input and the phosphor irradiance. This was achieved by a gamma fit[25] to a calibration curve obtained with a United Detector Technology Optometer (UDT S370) fitted with a radiometric detector (Model 260). Linearization was further improved by use of a straight-line fit of a second calibration of the LUT input to irradiance variation. Contrast errors were within 0.33 dB (0.017 log unit).

B. Procedure

All experiments were performed monocularly. A staircase-driven two-alternative forced-choice paradigm was used to measure thresholds. The grating appeared randomly in one of two 500-ms intervals, each signaled by a tone. The subject indicated by a mouse button press in which interval the grating appeared. Audio feedback was provided. An incorrect response raised the grating contrast by 2 dB (1 dB = 1/20 log unit), and two consecutive correct responses lowered the contrast by 1 dB. This choice of step size yielded a mean threshold at the 81.6% correct level.[26] The threshold value was taken as the arithmetic mean, in decibels, of the last six of the ten staircase reversals required for completion of each trial. At least three trials were performed for each data point, and trials were repeated until a standard error of 1.0 dB per datum was obtained.

Two- and three-dimensional threshold contours were plotted in cone contrast space (see below). The two-dimensional contours were obtained in each of three planes chosen to reveal the salient features of mechanisms in turn (Fig. 1). These planes were the (L, M) plane normal to the vector (0, 0, 1) and containing the L and M axes, the (L + M) plane normal to (1, −1, 0) and containing the L + M and S axes, and the (L − M) plane normal to (1, 1, 0) and containing the L − M and S axes. We chose the (L, M) plane to investigate the L- and M-cone weightings to the red–green and luminance mechanisms, the L + M plane to investigate the blue–yellow mechanism and S-cone inputs to the luminance mechanism, and the L − M plane to investigate S-cone inputs to the red–green mechanism. In each plane, thresholds were obtained along 12 equally spaced axes. Three-dimensional contours were also obtained from thresholds measured in 60 equally spaced axes in space, including the 34 axes used for the two-dimensional contours. Additional threshold measurements were made for both two- and three-dimensional contours in contour regions that were poorly sampled.

C. Cone Contrast Representation

Cone contrast is given by the increase $(\delta L, \delta M, \delta S)$ in the quantal catch of each cone type to the stimulus relative to the quantal catch (L_0, M_0, S_0) to the background.[7,8] We assume in using this space that the cones follow Weberian excitation, as supported by Chaparro *et al.*[27] for L and M cones. Cone contrast space permits direct estimation of mechanism's cone weightings from threshold contour parameters on the basis of a probability summation model.[28] As this is a contrast space, no arbitrary scaled units are introduced.

Cone quantal catch (E_L, E_M, E_S) and phosphor irradiances (E_R, E_G, E_B) are related by the linear transformation[29,30]

$$\begin{bmatrix} E_L \\ E_M \\ E_S \end{bmatrix} = \begin{bmatrix} \frac{\int r(\lambda)l(\lambda)\mathrm{d}\lambda}{\int r(\lambda)p(\lambda)\mathrm{d}\lambda} & \frac{\int g(\lambda)l(\lambda)\mathrm{d}\lambda}{\int g(\lambda)p(\lambda)\mathrm{d}\lambda} & \frac{\int b(\lambda)l(\lambda)\mathrm{d}\lambda}{\int b(\lambda)p(\lambda)\mathrm{d}\lambda} \\ \frac{\int r(\lambda)m(\lambda)\mathrm{d}\lambda}{\int r(\lambda)p(\lambda)\mathrm{d}\lambda} & \frac{\int g(\lambda)m(\lambda)\mathrm{d}\lambda}{\int g(\lambda)p(\lambda)\mathrm{d}\lambda} & \frac{\int b(\lambda)m(\lambda)\mathrm{d}\lambda}{\int b(\lambda)p(\lambda)\mathrm{d}\lambda} \\ \frac{\int r(\lambda)s(\lambda)\mathrm{d}\lambda}{\int r(\lambda)p(\lambda)\mathrm{d}\lambda} & \frac{\int g(\lambda)s(\lambda)\mathrm{d}\lambda}{\int g(\lambda)p(\lambda)\mathrm{d}\lambda} & \frac{\int b(\lambda)s(\lambda)\mathrm{d}\lambda}{\int b(\lambda)p(\lambda)\mathrm{d}\lambda} \end{bmatrix} \times \begin{bmatrix} E_R \\ E_G \\ E_B \end{bmatrix}, \quad (2)$$

where r, g, and b represent the measured spectral emission functions of the red, green, and blue phosphors, respectively; p represents the manufacturer-specified spectral sensitivity function of the calibrated head; and l, m, and s represent the Smith–Pokorny[31] cone spectral absorption functions. A grating was thus represented by a point (L, M, S) in cone contrast space given by the maximum quantal catch deviation of each cone type relative to the background. The spatiotemporal symmetry of the stimulus imposed a symmetry of all threshold data about the origin. The contrast C of the grating was defined as $(L^2 + M^2 + S^2)^{1/2}$, the magnitude of the stimulus vector. The postreceptoral mechanisms could also be represented by a point (L, M, S) in cone contrast space, where, in this case, L, M, and S represent the respective cone weights of the mechanism.

D. Superelliptical Fits

In our study the two-dimensional threshold contours were fitted by superellipses. These are curves of the form[32]

$$f(x, y) = \left| \frac{x}{a_x} \right|^{\beta} + \left| \frac{y}{a_y} \right|^{\beta} = 1. \quad (3)$$

The extent parameters a_x and a_y represent the lengths of the axes of the superellipse, with the x axis chosen to be the minor axis. The parameter β indicates the shape of the superellipse, with $\beta \to \infty$ producing a rectangle, $\beta > 2$

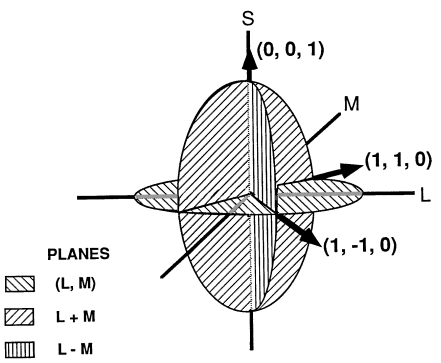

Fig. 1. Planes used for two-dimensional threshold contours in (L, M, S) space.

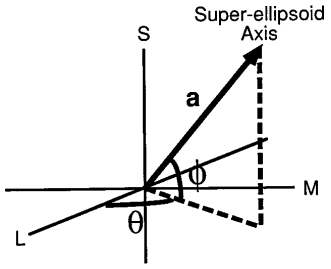

Fig. 2. Superellipsoid parameters. a, θ, and ϕ parameters for each axis (x, y, z) of the three-dimensional superellipsoid fits.

a squared superellipse, $\beta = 2$ a perfect ellipse, $1 < \beta < 2$ a piqued superellipse, and $\beta = 1$ a rhombus. In addition to these parameters the superelliptical fit has an orientation parameter ($\phi_{1,2,3}$), which is the orientation of the superellipse axes relative to some reference axes in each of the three planes.

Three-dimensional contours were fitted with superellipsoids having the form

$$f(x, y, z) = \left(\left| \frac{x}{a_x} \right|^{\beta_2} + \left| \frac{y}{a_y} \right|^{\beta_2} \right)^{\beta_1/\beta_2} + \left| \frac{z}{a_z} \right|^{\beta_1} = 1. \quad (4)$$

The extent parameters a_x, a_y, and a_z and the shape parameters β_1 and β_2 have properties analogous to those of the superellipse. The x axis was set to be the shortest axis, and z the longest. In addition to these parameters, the superellipsoid has six orientation parameters $(\theta, \phi)_{x,y,z}$ (Fig. 2). These represent the directions in spherical coordinates of the x, y, and z axes, respectively. The shape parameter β provides an estimate of the power of summation from the probability summation model (App. A), which is also the slope of the Weibull fit to the psychometric detection function.[11] All fits were made by Levenburg–Marquardt volume minimization.[33] This technique minimizes the sum of the squares of an error metric D, given by

$$D = (a_x a_y a_z)^{1/2} [f^{\epsilon_1}(x, y, z) - 1]. \quad (5)$$

This technique will generally lead to extent values that are lower than those obtained by a least-squares fit.

On the basis of a probability summation model[11,28] we estimated the cone weightings of the most-sensitive mechanisms when the ratio of the axis lengths of the contours was high. In this case the shortest axis of the contour yielded an estimate of the vector representing the most-sensitive mechanism (Fig. 3), within the theoretic directional uncertainty calculated in Appendix A. The other contour axes yielded partial information on the sensitivities and magnitudes of the other mechanisms (Fig. 3). Whenever possible, we improved the estimate of the direction of the most-sensitive mechanism by using the calculation shown in Appendix A (see Section 4).

E. Observers

Three observers, MS, DD, and AW, were used in the experiments. All observers wore their optical corrections and tested normally on the Farnsworth–Munsell 100-hue test for color vision. Only observer MS was an experienced observer.

3. RESULTS

A. Mid-Spatial, Low-Temporal Condition: *SF* = 1 c/deg, *TF* = 0 Hz

Figure 4 shows the detection thresholds (±1 standard deviation) for the three subjects in the (1 c/deg, 0 Hz) condition. The axes in all plots are in units of cone contrast. The corresponding parameters of the fit contours are shown in the top three rows of Table 1. We note that in this, and all other, conditions the orientation parameters show lower intersubject variation than the extent parameters do. This illustrates that the intersubject variability in the cone-weight ratios is lower than that of the corresponding sensitivities.

The top row of panels of Fig. 4 shows the results in the (L, M) plane. All subjects show a flattened superellipse ($\beta = 4.0 \pm 0.3$) with its minor axis oriented at a mean value of ϕ_1 (the orientation of the minor axis relative to the L axis) = −42.3°. This indicates a sensitive mechanism with equal weightings of L and M cones in opposition, indicative of the red–green mechanism.

In the L + M plane (Fig. 4, middle row of panels) the minor axis is oriented along the L + M axis [mean ϕ_2 (the orientation of the minor axis relative to the L + M axis) = −2.9°], and the contour is elongated along the major (S) axis. This shows that the summing mechanism of L and M inputs has an S-cone input of 5% of the total in opposition to L and M cones and that the third S-modulated mechanism is of relatively low sensitivity in this condition.

In the L − M plane (Fig. 4, bottom row of panels) the minor axis lies along the L − M axis [mean ϕ_3 (the orientation of the minor axis relative to the L − M axis) = −0.7°]. This shows that the sensitive red–green mechanism has an S-cone input of 1% in support of M cones.

The three-dimensional plots for the three subjects are shown in Fig. 5. The three-dimensional fits to additional

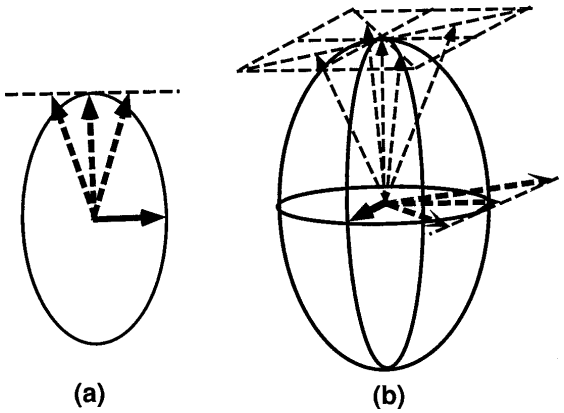

Fig. 3. Mechanism estimation from detection contours. (a) For two-dimensional contours the shorter axis approximates the vector representing the more-sensitive mechanism (solid arrow). The longer axis constrains the vector representing the less-sensitive vector (dashed arrows) to the contour tangent (dashed line). (b) In the three-dimensional case, the short axis again approximates the vector of the most-sensitive mechanism (solid arrow). The second-longest axis constrains the second-most-sensitive mechanism (thick dashed arrows) to a tangential line (horizontal thick dashed line). The longest axis constrains the least-sensitive mechanism (thin dashed arrows) to a tangential plane (thin dashed grid).

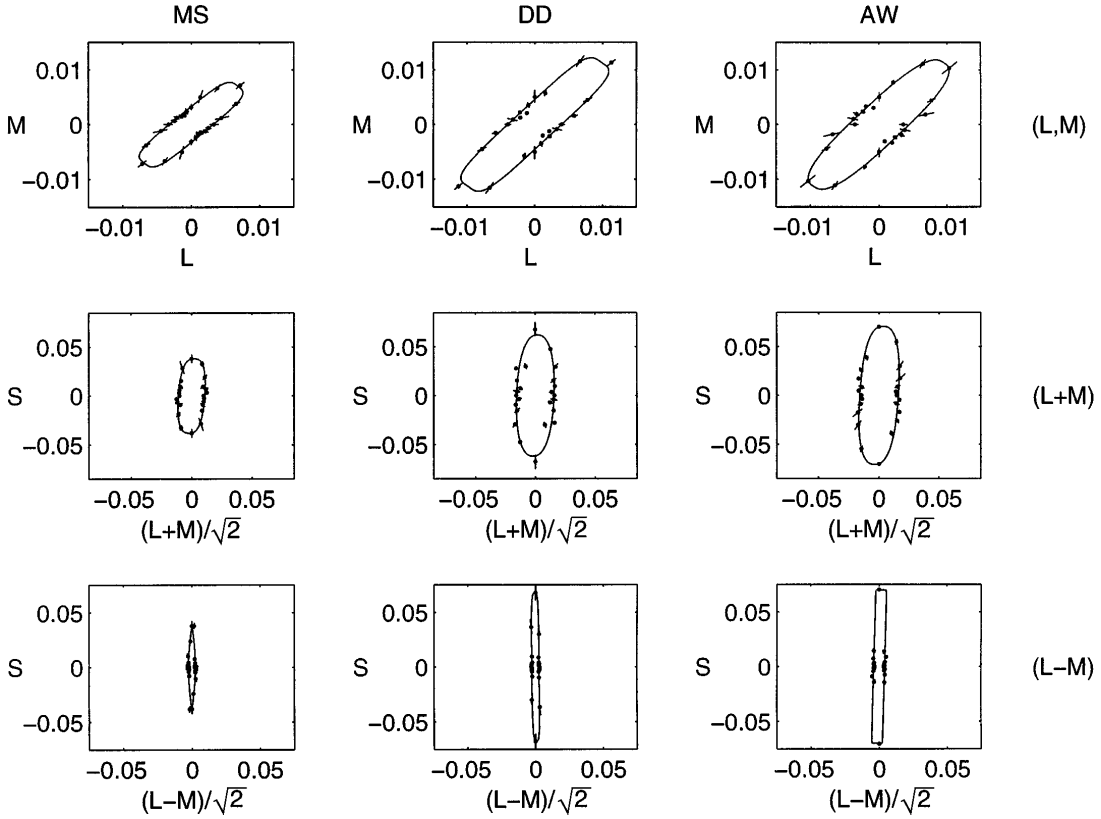

Fig. 4. Two-dimensional contours for (1 c/deg, 0 Hz). Threshold contours in three planes (rows) for three subjects (columns). Axes are in units of cone contrast. Error bars represent standard deviations.

data in equally spaced directions permit us to verify the features shown in the two-dimensional plots without making *a priori* assumptions about test directions.

The corresponding fit parameters are shown in the top three rows of Table 2. The orientation parameters $(\theta, \phi)_{x,y,z}$ are defined in Fig. 2. The x-axis orientation parameters (mean value $\theta_x = -42.5$, $\phi_x = -2.0°$) reveal a sensitive mechanism having an L − M-cone input in balanced opposition and an S-cone input of 3% in support of M cones. The y axis is in the ($\theta_y = 47.6$, $\phi_y = 3.2°$) direction, indicating that the second-most-sensitive mechanism sums L- and M-cone inputs in some indeterminate ratio and has 6% S-cone inputs in opposition to L and M cones. The longest axis is oriented close to the S axis ($\theta_z = 20.3$, $\phi_z = 86.0°$) and confirms that the S-modulated mechanism is less sensitive than the other two mechanisms in this condition.

B. Low-Spatial, Low-Temporal Condition: *SF* = 0.125 c/deg, *TF* = 0 Hz

Figure 6 (top row of panels) shows the results in the (L, M) plane for the (0.125 c/deg, 0 Hz) condition, with

Table 1. Two-Dimensional Fit Parameters[a]

	(L, M) Plane				(L+M) Plane				(L−M) Plane			
Subject	a_x/%	a_y/%	ϕ_1/°	β	a_x/%	a_y/%	ϕ_2/°	β	a_x/%	a_y/%	ϕ_3/°	β
Mid-spatiotemporal condition: 1 c/deg; 0 Hz												
MS	0.23	0.98	−44.3	3.9	1.07	3.82	−3.6	2.6	0.27	3.71	−0.1	1.3
DD	0.30	1.50	−41.0	4.3	1.56	6.22	−1.9	2.3	0.27	6.74	−0.5	3.9
AW	0.34	1.37	−41.5	3.7	1.60	7.10	−3.1	2.5	0.40	7.00	−1.3	⋆
Low-spatial condition: 0.125 c/deg; 0 Hz												
MS	0.22	1.68	−43.1	1.6	1.09	3.42	−55.4	9.5	0.19	1.29	0.9	3.0
DD	0.26	2.50	−43.0	⋆	1.65	2.89	−49.1	2.7	0.23	2.03	0.0	1.2
AW	0.49	3.74	−43.1	⋆	3.47	11.0	−45.9	1.8	0.51	3.64	2.4	2.7
High-temporal condition: 1 c/deg; 24 Hz												
MS	4.18	10.8	14.0	2.99								
DD	4.64	12.4	7.1	2.27								
AW	6.15	15.0	12.2	1.90								

[a]The extent parameters ($a_{x,y}$) are quoted in percent cone contrast units. $\phi_{1,2,3}$ represents the orientation of the minor axis relative to the L, L + M, and L − M axes in the (L, M), (L + M) and (L − M) planes, respectively. ⋆ indicates that the shape parameter β converged to the highest allowable value and was rejected.

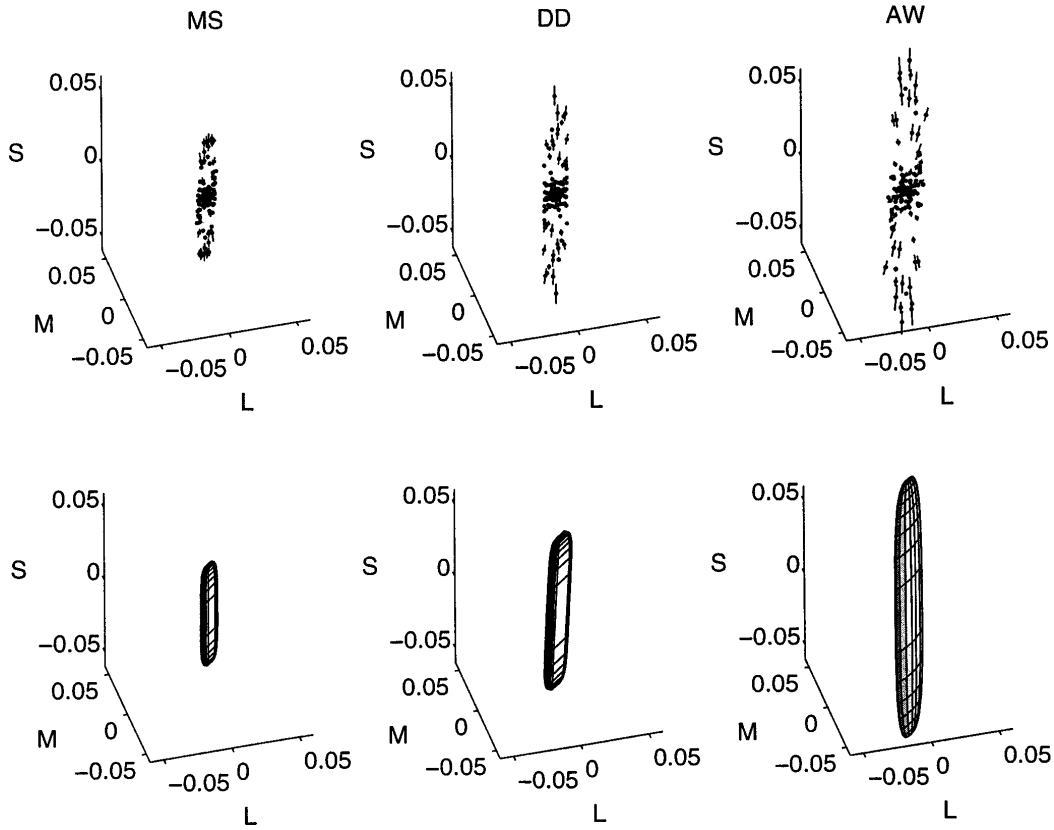

Fig. 5. Three-dimensional contours for (1 c/deg, 0 Hz). Thresholds (top panels) and fit contours (bottom panels) for three subjects (columns). Axes are in units of cone contrast.

the accompanying fit parameters shown in the middle three rows of Table 1. The contours are squared ellipses as in the mid-spatiotemporal condition, having a mean orientation $\phi_1 = -43.1°$. As in the previous condition, these results support the existence of a sensitive L − M mechanism and show that the balanced cone weightings to this mechanism are not affected by the shift in spatial frequency. The y axis is now noticeably longer than in the mid-spatiotemporal condition (mean $a_y = 26.4 \times 10^{-3}$ versus 12.2×10^{-3}). This illustrates that the luminance mechanism is less sensitive at lower spatial frequencies.

The results in the L + M plane are shown in Fig. 6 (middle row of panels). These contours maintain the same shape as in the (1 c/deg, 0 Hz) condition but with an approximately 45° rotation (mean $\phi_2 = -50.1°$ versus $-2.9°$). This shows that the contour in this condition is affected primarily by a new mechanism with a larger S-cone input. This value of ϕ_2 is now close to the value of $-54.7°$ expected from a perfectly balanced blue–yellow mechanism. It illustrates the action of such a mechanism and agrees with earlier results[16] that indicate that the sensitivity of the blue–yellow mechanism relative to that of the luminance mechanism is much higher at 0.125 than at 1 c/deg.

The contours in the L − M plane (Fig. 6, bottom row of panels) are elongated superellipses oriented at mean $\phi_3 = 1.1°$. This shows that the red–green mechanism has a 2% S-cone input as in the (1 c/deg, 0 Hz) case but now in support of L cones. The major axis—oriented close to the S axis—in this condition is significantly shorter than that in the previous condition ($a_y = 23.1 \times 10^{-3}$ and 58.2×10^{-3}, respectively). This confirms that the S-modulated blue–yellow mechanism is more sensitive in this condition.

Table 2. Three-Dimensional Fit Parameters[a]

Subject	a_x/%	a_y/%	a_z/%	θ_x/°	ϕ_x/°	θ_y/°	ϕ_y/°	θ_z/°	ϕ_z/°	β_1	β_2
Mid-spatiotemporal condition: 1 c/deg; 0 Hz											
MS	0.23	1.03	3.34	−44.0	−1.1	46.1	−2.8	24.6	87.0	4.2	4.3
DD	0.28	1.43	5.00	−42.6	−4.3	47.7	−3.4	−4.2	84.5	5.3	7.4
AW	0.40	2.11	8.50	−41.0	−0.5	49.0	−3.4	40.6	86.6	3.3	1.7
Low-spatial condition: 0.125 c/deg; 0 Hz											
MS	0.20	1.09	2.84	−31.2	−35.2	87.6	−34.4	27.7	39.6	4.7	1.9
DD	0.22	1.59	4.91	−29.4	−32.9	85.6	−33.1	28.2	39.6	1.5	2.2
AW	0.49	3.25	9.06	−35.8	−27.4	70.9	−29.0	19.0	48.1	4.1	2.7

[a] a, θ, and ϕ parameters are illustrated in Fig. 2. Extent parameters ($a_{x,y,z}$) are quoted in % cone contrast units.

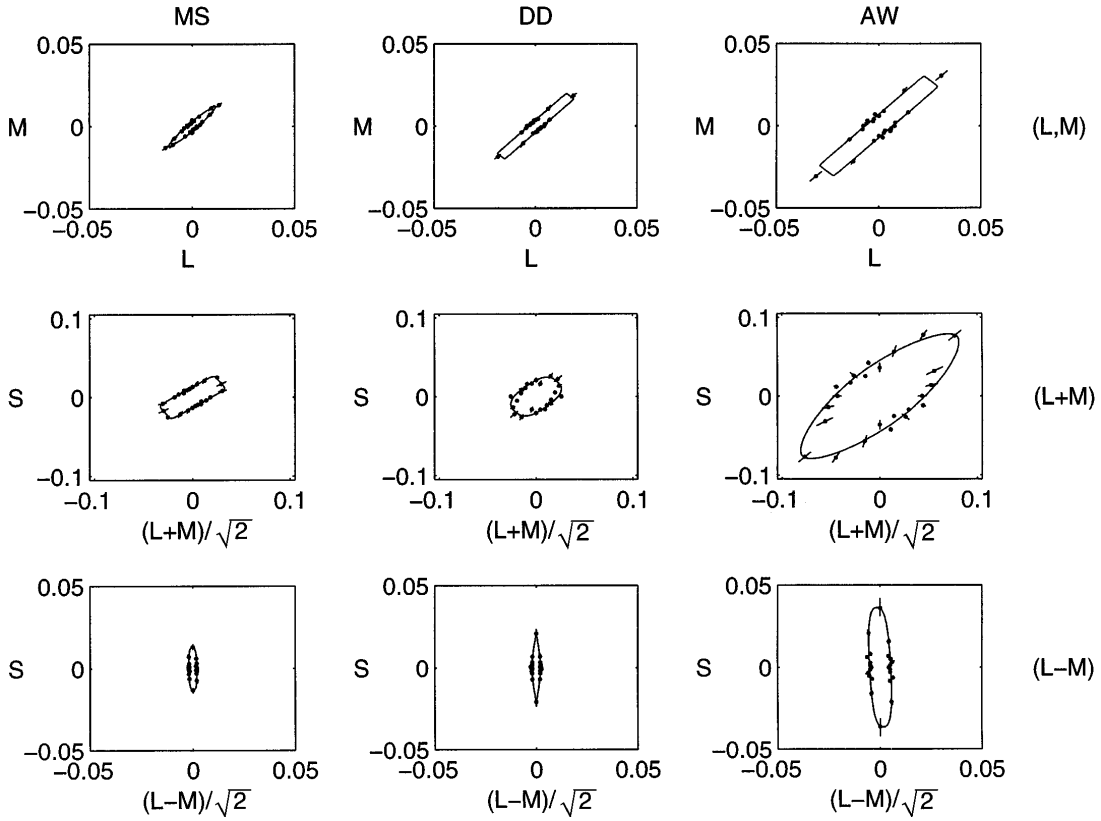

Fig. 6. Same as Fig. 4 but for two-dimensional contours for (0.125 c/deg, 0 Hz).

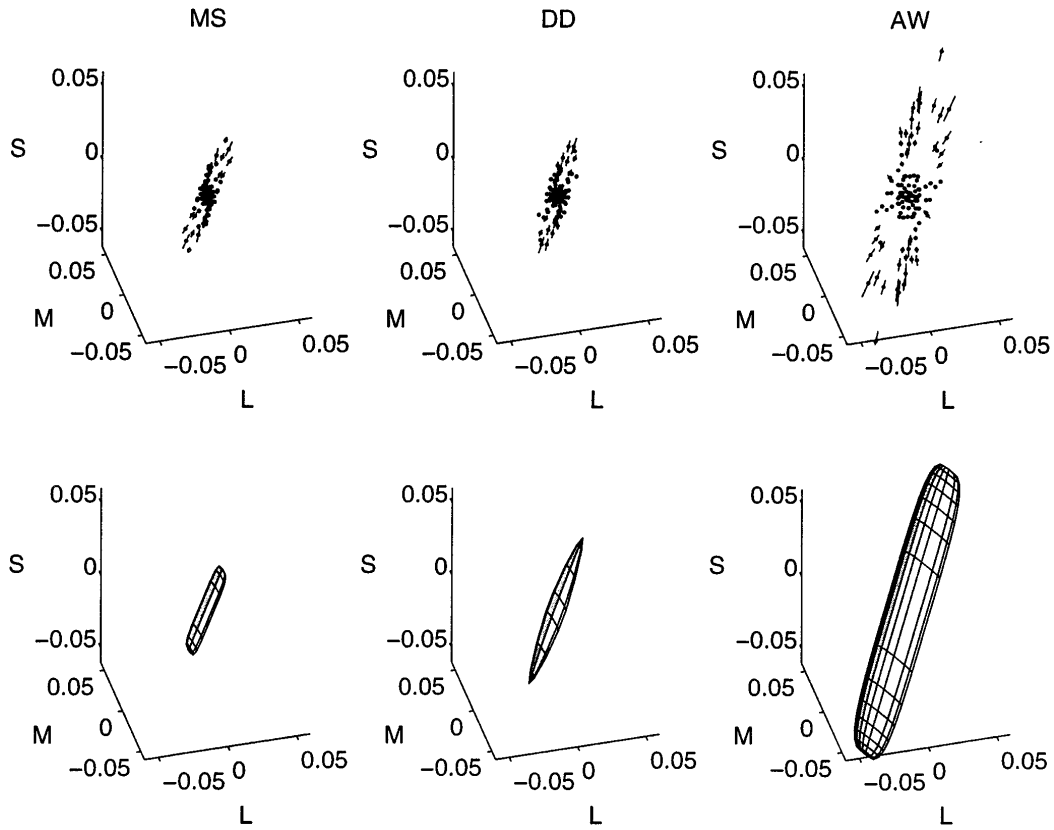

Fig. 7. Same as Fig. 5 but for three-dimensional contours for (0.125 c/deg, 0 Hz).

Table 3. Cone-Weight Estimates[a]

Observer	θ/°	ϕ/°	L	M	S
Red–green					
	(1 c/deg, 0 Hz)	(1 c/deg, 0 Hz)			
MS	−44.3 ± 0	−1.1 ± 1	0.72	−0.70	−0.02
DD	−41.0 ± 0	0.5 ± 0	0.75	−0.66	0.01
AW	−41.5 ± 0	−1.3 ± 0	0.75	−0.66	−0.02
Blue–yellow					
		(0.125 c/deg, 0 Hz)			
MS	–	−55.4 ± 0 (−55.4)	0.40[b]	0.40[b]	−0.82
DD	–	−49.1 ± 16 (−60.8)	0.34[b]	0.34[b]	−0.87
AW	–	−45.9 ± 23 (−53.0)	0.42[b]	0.42[b]	−0.80
Luminance					
	(1 c/deg, 24 Hz)	(1 c/deg, 0 Hz)			
MS	14.0 ± 4 (17.3)	−3.6 ± 5	0.95	0.30	−0.06
DD	7.1 ± 15 (12.2)	−1.9 ± 8	0.98	0.21	−0.03
AW	12.2 ± 24 (18.7)	−3.1 ± 5	0.95	0.32	−0.05

[a] θ and ϕ represent directions in spherical coordinates and are shown for the spatiotemporal conditions indicated. Errors denote imprecision in raw data (see text). Reevaluated estimates appear in parentheses. (L, M, S) represent transformation of the most precise estimates to normalized L-, M-, and S-cone weights.
[b] L- and M-cone inputs to the blue–yellow mechanism were indeterminate and assumed to be equal.

The three-dimensional plots for the low-spatial condition are shown in Fig. 7, with the corresponding fit parameters in the bottom three rows of Table 2. The orientation parameters differ from those in the mid-spatiotemporal condition. The shortest axis ($\theta_x = -32.1°$, $\phi_x = -31.8°$; Table 2) no longer lies in the (L, M) plane, illustrating the relative sensitization of the S-modulated blue–yellow mechanism in this condition. The z axis ($\theta_z = 25.0°$, $\phi_z = 42.4°$) is now oriented in the vicinity of the achromatic axis ($\theta = 45.0°$, $\phi = 35.3°$), suggesting that the two most-sensitive mechanisms, the red–green and the blue–yellow mechanisms, are chromatic, i.e., have balanced cone inputs. The high sensitivity of the red–green mechanism, however, makes it difficult to estimate the relative L- and M-cone inputs to the blue–yellow mechanism.

C. Mid-Spatial, High-Temporal Condition: *SF* = 1 c/deg, *TF* = 24 Hz

Figure 8 illustrates the (1 c/deg, 24 Hz) condition contours in the (L, M) plane for three subjects. The corresponding fit parameters are shown in the bottom three rows of Table 1. The contours are squared ellipses as before. They are, however, much larger (by a factor of 8) than in the previous conditions, indicating that the sensitivities of all mechanisms are significantly reduced. Their orientations for the three subjects are $\phi_1 = 7.1°$, 12.2°, 14.0°. This reveals a relatively sensitized mechanism consisting of an additive combination of L and M cones. This is consistent with previous results that the sensitivity of the luminance mechanism declines more slowly than that of the other two mechanisms with increased temporal frequency. Our results demonstrate that the luminance mechanism is dominated by L-cone inputs by a factor of 4–8 times relative to M-cone inputs.

4. DISCUSSION

Table 3 summarizes the estimated vector direction (θ, ϕ) in (L, M, S) space for the three postreceptoral mechanisms as obtained from the orientations of the minor axes of the relevant contours. In this table these estimates have been drawn from the three spatiotemporal conditions, as shown. For any given contour the direction estimate can be specified only within a certain range of precision $\pm\epsilon$ (the error value in Table 3, calculation in Appendix A) because of the unspecified effect of the less-sensitive mechanism. This precision increases as the major/minor-axis ratio increases, indicating that the less-sensitive mechanism is becoming relatively less sensitive, and as the shape parameter β increases, in which case the region of the contour near the minor axis approaches a straight line of definite slope.

If, however, the vector direction of the less-sensitive mechanism is known, that of the more sensitive mechanism can be determined precisely. This determination is achieved by comparison of the theoretical and measured threshold contours and solution for the unknown mechanism direction (Appendix A). We thus obtain new estimates (shown in parentheses in Table 3) in two cases in which the precision of the original estimate was low. We reevaluated the ϕ estimate of the blue–yellow mechanism, using the precisely estimated ϕ value ($\phi = 0$) of the luminance mechanism, and likewise recomputed the θ estimate of luminance estimate, using the precisely obtained $\theta = -45°$ red–green estimate.

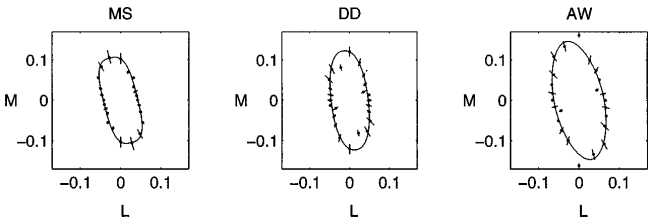

Fig. 8. Same as Fig. 4 but for two-dimensional (L, M) contours for (1 c/deg, 24 Hz).

The results of these reevaluations of the mechanism directions are shown in parentheses in Table 3. The overall results, with the reevaluated angles, are transformed into an (L, M, S) representation to show the actual normalized cone weights. The results confirm that the red–green mechanism has balanced opponent inputs of L and M cones with little or no S-cone input, the blue–yellow mechanism has S-cone inputs in balanced opposition to an indeterminate combination of L and M cones, and the luminance mechanism sums L- and M-cone inputs, with little or no S-cone input, in a subject-dependent ratio that lies between 3 and 5 for the (1 c/deg, 24 Hz) condition.

These results agree with earlier findings[7–11,34] for which different but related techniques were used. Noorlander *et al.*[7] and Noorlander and Koenderink[8] fitted ellipses/ellipsoids to threshold contours for gratings and obtained parameters in close agreement with ours for the low-temporal conditions. Stromeyer *et al.*[9,10] and Chaparro *et al.*,[12] using spot stimuli, found that the red–green mechanism has an exact L − M-cone weighting under a range of spatiotemporal conditions. Cole *et al.*[11] estimated that the red–green mechanism for 2° spots had an exact L − M-cone weighting, although another study[35] showed small S-cone inputs to this mechanism. Our results also agree with those of Cole *et al.*[11] and with other psychophysical results obtained with drifting gratings[4–6] that the luminance mechanism has only small S-cone inputs. Furthermore, we have specified the cone weightings of the blue–yellow mechanism with a greater precision than in previous studies.

Our method differs from the methods of these previous studies in several important respects. Noorlander and Koenderink[8] obtained three-dimensional contours from only 16 data points in cone contrast space. In addition, our squared elliptical contours ($\beta > 2$) enabled us to obtain more-precise estimates than did the best-fitting ellipse. Stromeyer *et al.*[9,10] and Chaparro *et al.*[12] restricted themselves to the (L, M) plane and therefore did not attempt to investigate either the S-modulated blue–yellow mechanism or the S inputs to the other mechanisms. Cole *et al.*[11] made threshold measurements in only the three principal planes and based their three-dimensional fits on these measurements. Our three-dimensional fits were obtained from a more uniform sampling using threshold measurements in equally spaced directions. In addition, our use of grating stimuli (unlike in previous studies[9,11,12]) permitted better isolation of mechanisms tuned to a particular spatiotemporal passband. We were thus able to alter spatial and temporal frequency to reveal the responses of individual mechanisms.

We have also shown that cone weightings of the red–green mechanism do not differ between the (1 c/deg, 0 Hz) and (0.125 c/deg, 0 Hz) conditions. This supports earlier studies showing small changes in mechanism weightings both across spatiotemporal conditions and across subjects.[8,11,12] However, care must be exercised in extending all our cone-weighting estimates across spatiotemporal conditions. For example, a phase lag between L and M cones is thought to vary the effective cone contributions to the luminance mechanism with temporal frequency under certain conditions.[36] In one study this variable phase lag led to an average reduction in the L/M ratio of the luminance motion mechanism from 3.5 to 1.5 as temporal frequency increased from 1 to 20 Hz.[37] Thus we cannot extrapolate cone weightings for the luminance mechanism across spatiotemporal conditions.

The L/M cone weight ratio that we obtained for the luminance mechanism (3–5) is higher than that obtained in another study (1.5) that used a similar technique.[37] This may simply be due to intersubject variability or to differences in the mean chromaticity (white versus yellow) that have been shown to affect the L/M ratio of the luminance mechanism.[36] It may also be due to the methods used to perform the fit, since the cited study fitted a segment of the contour with a straight line. Such a fit for subject AW (Fig. 8) can produce an L/M ratio of less than 2.

Several sources of error have been considered in our experiments. We used Smith–Pokorny[31] primaries, which are psychophysically derived and based on averaged results over a number of observers. Despite the fact that all our subjects scored normally on the Farnsworth–Munsell 100-hue test, some variation in cone primaries is likely to occur among individual subjects. Cole *et al.*[11] calculated, however, that their results would be accurate with shifts in the cone primaries of up to 10 nm. Inasmuch as our method is based on the same basic technique, the same conclusion applies. We also concern ourselves with the symmetry about the origin in cone contrast space imposed by our choice of stimulus. Results from Stromeyer *et al.*[9] and Cole *et al.*[11] show, however, that mechanisms generally show symmetric behavior, at least in the fovea.

Another possible source of error arises from the choice of fit. The unbiased chi squared[8] for the three-dimensional superellipsoids was less by a factor of 1.05–1.25 than the best-fitting ellipsoid to the three-dimensional data. However, this fact was insufficient to permit us to conclude (F-test, $\alpha = 0.05$) that the superellipsoid was a better model. The standard deviations of the individual measurements are small (~10% in contrast units) relative to the magnitudes of the threshold vectors. The large standard deviations of data in the regions of the contour farthest from the origin were of little consequence because points in these regions were least indicative of the cone weighting of the most-sensitive mechanism.

The shape parameter β is an estimate of the slope parameter of the Weibull fit to the psychometric function.[11] We obtained an average β of 3.25 ± 0.33 over all contours and spatiotemporal conditions. Previous estimates of the Weibull slope from contour measurements yielded values between 3.5 and 4.8.[11,30] These are higher than the slopes (~2) obtained from direct measurement of the psychometric function.[11] This may be due to reductions in these slope estimates that are due to observer variation.[38] Our estimate does not appear to vary considerably with the orientation of the contour plane, in agreement with Maloney,[38] although Stromeyer *et al.*[39] found that β differs between the luminance and red–green mechanisms. Our results may, however, suggest a reduction of β for the high-temporal condition (2.39 ± 0.32) compared with the mid-spatiotemporal condition (3.62 ± 0.42). Small differences in these estimates cannot be considered reliable,

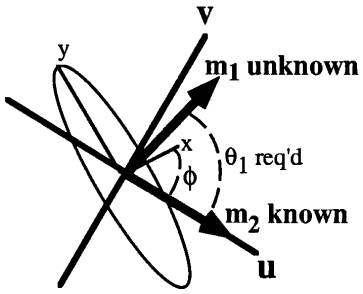

Fig. 9. Notation: Appendix A.

however, owing to the high variance of β that is due to sparse sampling at regions of the contour farthest from the origin, especially for elongated contours.

The fact that β was greater than 2 in most cases confirms that the contours were generally squared ellipses. This, combined with the goodness of fit noted above, suggests that each planar contour was influenced largely by two mechanisms and that the three-dimensional contours were affected by three mechanisms, as each flattened edge or face would represent the influence of a single mechanism.[9] This therefore supports a three-mechanism model. In addition, estimates of the cone weights determined directly from the orientation of the superellipse contour are more precise than those for the best-fitting ellipse ($\beta = 2$) because, as mentioned above, this precision increases with β.

APPENDIX A: PRECISE ESTIMATION OF THE CONE-WEIGHT RATIOS

To derive the direction in a given plane of a mechanism $\mathbf{m}_1$ (Fig. 9), given the direction of a second, less-sensitive mechanism $\mathbf{m}_2$, we compare the coefficients of the series expansion for the probability summation model and that for the fitted superellipse. This gives an exact derivation in the elliptic case ($\beta = 2$) and an approximate derivation for all other values of β.

A probability summation model[28] for threshold detection gives the planar threshold contour $\mathbf{p}$:

$$\sum_i |\mathbf{m}_1\mathbf{p}|^\beta = 1, \tag{A1}$$

where $\mathbf{m}_i(m_{u,i}, m_{v,i})$ is the planar projection of the ith mechanism vector in some arbitrary coordinate system (u, v) in the plane (Fig. 9). To simplify the calculation, we choose (u, v) such that the u axis is aligned with $\mathbf{m}_2$, i.e., $m_{v,2} = 0$.

The model can be expressed as

$$(m_{u,1}u + m_{v,1}v)^\beta + (m_{u,2}u + m_{v,2}v)^\beta = 1, \tag{A2}$$

which, expressed as a power series to three terms for small v/u, is

$$(m_{u,1}u)^\beta\left[1 + \beta\left(\frac{m_{v,1}v}{m_{u,1}u}\right) + \frac{\beta(\beta-1)}{2!}\left(\frac{m_{v,1}v}{m_{u,1}u}\right)^2\right] + (m_{u,2}u)^\beta\left[1 + \beta\left(\frac{m_{v,2}v}{m_{u,2}u}\right) + \frac{\beta(\beta-1)}{2!}\left(\frac{m_{v,2}v}{m_{u,2}u}\right)^2\right] = 1. \tag{A3}$$

For the fitted contour, let $a_x = 1/k_x$ and $a_y = 1/k_y$ represent the lengths of the minor and major axes, respectively, of the fit and ϕ the orientation of the minor axis relative to the u axis. The equation of the fit is then

$$[(k_x \cos\phi)u + (k_x \sin\phi)v]^\beta + [(k_y \sin\phi)u - (k_y \cos\phi)v]^\beta = 1. \tag{A4}$$

Expanding to three terms for small v/u,

$$[k_x(\cos\phi)u]^\beta\left\{1 + \beta\left[\frac{k_x(\sin\phi)v}{k_y(\cos\phi)u}\right] + \frac{\beta(\beta-1)}{2!} \times \left[\frac{k_x(\sin\phi)v}{k_x(\cos\phi)u}\right]^2\right\} + (k_y(\sin\phi)u)^\beta\left\{1 - \beta\left[\frac{k_y(\cos\phi)v}{k_y(\sin\phi)u}\right] + \frac{\beta(\beta-1)}{2!}\left[\frac{k_y(\cos\phi)v}{k_y(\sin\phi)u}\right]^2\right\} = 1, \tag{A5}$$

we compare coefficients of $(v/u)^0$, $(v/u)^1$, and $(v/u)^2$ between Eqs. (A3) and (A5) for small v/u. This is justified because the u axis is close to the minor axis of the contour, which is our most heavily sampled region:

$$m_{u,1}{}^\beta + m_{u,2}{}^\beta = (k_x \cos\phi)^\beta + (k_y \sin\phi)^\beta, \tag{A6}$$

$$m_{u,1}^\beta\left(\frac{m_{v,1}}{m_{u,1}}\right) + m_{u,2}^\beta\left(\frac{m_{v,2}}{m_{u,2}}\right) = (k_x \cos\phi)^\beta\left(\frac{\sin\phi}{\cos\phi}\right) - (k_y \sin\phi)^\beta\left(\frac{\cos\phi}{\sin\phi}\right), \tag{A7}$$

$$m_{u,1}^\beta\left(\frac{m_{v,1}}{m_{u,1}}\right)^2 + m_{u,2}^\beta\left(\frac{m_{v,2}}{m_{u,2}}\right)^2 = (k_x \cos\phi)^\beta\left(\frac{\sin\phi}{\cos\phi}\right)^2 + (k_y \sin\phi)^\beta\left(\frac{\cos\phi}{\sin\phi}\right)^2. \tag{A8}$$

Put $m_i(m_{u,1}, m_{v,1}) = (S_i \cos\theta_i, S_i \sin\theta_i)$. Recall that, from our choice of (u, v), $m_{v,2} = 0$. Thus $\theta_2 = 0$, and the θ_1 = direction of m_1 relative to m_2 is given from Eqs. (A7) and (A8) by

$$\tan\theta_1 = \frac{m_{v,1}}{m_{u,1}} = \frac{(k_x \cos\phi)^\beta\left(\frac{\sin\phi}{\cos\phi}\right)^2 + (k_y \sin\phi)^\beta\left(\frac{\cos\phi}{\sin\phi}\right)^2}{(k_x \cos\phi)^\beta\left(\frac{\sin\phi}{\cos\phi}\right) - (k_y \sin\phi)^\beta\left(\frac{\cos\phi}{\sin\phi}\right)}. \tag{A9}$$

In general, the largest discrepancy $\epsilon = |\phi - \theta_1|$ between the direction of the minor axis and that of the most-sensitive mechanism occurs when the mechanisms are equiangular to the minor axis, i.e., $\theta_1 = 2\phi \Rightarrow \epsilon = |\phi'|$, which can be solved for in Eq. (A9) by iteration.

ACKNOWLEDGMENTS

We thank William McIlhagga for his constructive comments and Frank Ferrie, Peter Whaite, and Duncan Baird for the fit software. This research was funded by a grant from the Medical Research Council of Canada (MT-10819).

REFERENCES

1. H. G. Sperling and R. S. Harwerth, "Red–green cone interactions in the increment-threshold spectral sensitivity of primates," Science **172,** 180–184 (1971).
2. J. E. Thornton and E. N. Pugh, Jr., "Red/green color opponency at detection threshold," Science **219,** 191–193 (1983a).
3. J. E. Thornton and E. N. Pugh, Jr., "Relationship of opponent-colours cancellation measures to cone-antagonistic signals deduced from increment threshold data," in *Colour Vision: Physiology and Psychophysics*, J. D. Mollon and L. T. Sharpe, eds. (Academic, London, 1983), pp. 362–373.
4. A. Eisner and D. I. A. MacLeod, "Blue sensitive cones do not contribute to luminance," J. Opt. Soc. Am. **70,** 121–123 (1980).
5. P. Cavanagh, D. I. A. MacLeod, and S. M. Anstis, "Equiluminance: Spatial and temporal factors and the contribution of blue-sensitive cones," J. Opt. Soc. Am. A **4,** 1428–1438 (1987).
6. J. Lee and C. F. Stromeyer III, "Contribution of human short-wave cones to luminance and motion detection," J. Physiol. **413,** 563–593 (1989).
7. C. Noorlander, M. J. G. Heuts, and J. J. Koenderink, "Sensitivity to spatiotemporal combined luminance and chromaticity contrast," J. Opt. Soc. Am. **71,** 453–459 (1981).
8. C. Noorlander and J. J. Koenderink, "Spatial and temporal discrimination ellipsoids in color space," J. Opt. Soc. Am. **73,** 1533–1543 (1983).
9. C. F. Stromeyer III, G. R. Cole, and R. E. Kronauer, "Second-site adaptation in the red–green chromatic pathways," Vision Res. **25,** 219–237 (1985).
10. C. F. Stromeyer III, G. R. Cole, and R. E. Kronauer, "Chromatic suppression of cone inputs to the luminance flicker mechanism," Vision Res. **27,** 1113–1137 (1987).
11. G. R. Cole, T. Hine, and W. McIlhagga, "Detection mechanisms in L-, M-, and S-cone contrast space," J. Opt. Soc. Am. A **10,** 38–51 (1993).
12. A. Chaparro, C. F. Stromeyer III, R. E. Kronauer, and R. T. Eskew, Jr., "Separable red–green and luminance detectors for small flashes," Vision Res. **34,** 751–762 (1994).
13. P. E. King-Smith, A. J. Vingrys, and S. C. Benes, "Visual thresholds measured with color video monitors," Color Res. Appl. **12,** 73–80 (1987).
14. A. B. Poirson and B. A. Wandell, "The ellipsoidal representation of spectral sensitivity," Vision Res. **30,** 647–652 (1990).
15. A. B. Poirson, B. A. Wandell, D. C. Varner, and D. H. Brainard, "Surface characterizations of color thresholds," J. Opt. Soc. Am. A **7,** 783–789 (1990).
16. D. G. Green, "Contrast sensitivity of colour mechanisms of the human eye," J. Physiol. **196,** 415–429 (1968).
17. C. R. Cavonius and O. Estevez, "Contrast sensitivity of individual colour mechanisms of human vision," J. Physiol. **248,** 649–662 (1975).
18. D. H. Kelly, "Spatiotemporal variation of chromatic and achromatic contrast thresholds," J. Opt. Soc. Am. **73,** 742–750 (1983).
19. K. T. Mullen, "The contrast sensitivity of human colour vision to red–green and blue–yellow chromatic gratings," J. Physiol. **359,** 381–400 (1985).
20. K. T. Mullen and J. C. Boulton, "Absence of smooth motion perception in color vision," Vision Res. **32,** 483–488 (1992).
21. J. G. Robson, "Spatial and temporal contrast-sensitivity functions of the visual system," J. Opt. Soc. Am. **56,** 1141–1142 (1966).
22. D. H. Kelly, "Motion and vision. II. Stabilized spatiotemporal threshold surface," J. Opt. Soc. Am. **69,** 1340–1349 (1979).
23. D. I. Flitcroft, "The interactions between chromatic aberration, defocus and stimulus chromaticity: Implications for visual physiology and colorimetry," Vision Res. **29,** 349–360 (1989).
24. A. Bradley, L. Zhang, and L. N. Thibos, "Failures of isoluminance caused by ocular chromatic aberration," Appl. Opt. **31,** 3657–3667 (1992).
25. D. G. Pelli and L. Zhang, "Accurate control of contrast on microcomputer displays," Vision Res. **31,** 1337–1350 (1991).
26. M. J. Sankeralli, "A quantitative analysis of normal postreceptoral chromatic mechanisms and its application to visual dysfunction," Master's thesis (McGill University, Montreal, Quebec, Canada, 1994).
27. A. Chaparro, C. F. Stromeyer III, G. Chen, and R. E. Kronauer, "Human cones appear to adapt at low light levels: measurements on the red–green detection mechanism," Vision Res. **35,** 3103–3118 (1995).
28. R. F. Quick, "A vector-magnitude model for contrast detection," Kybernetic **16,** 65–67 (1974).
29. G. R. Cole and T. J. Hine, "Computation of cone contrasts for color vision research," Behav. Res. Methods Instrum. Comp. **24,** 22–27 (1992).
30. A. J. Vingrys, A. B. Metha, and D. R. Badcock, "Modeling post receptoral mechanisms with cone contrast," Invest. Ophthalmol. Vis. Sci. **34,** 750 (1993).
31. V. C. Smith and J. Pokorny, "Spectral sensitivity of the foveal photopigments between 400 and 500 nm," Vision Res. **15,** 161–171 (1975).
32. A. H. Barr, "Superquadrics and angle preserving transformations," IEEE Comput. Graphics Appl. **1,** 11–23 (1981).
33. P. Whaite and F. P. Ferrie, "From uncertainty to visual exploration," IEEE Trans. PAMI **13,** 1038–1049 (1991).
34. A. B. Metha, A. J. Vingrys, and D. R. Badcock, "Detection and discrimination of moving stimuli: the effects of color, luminance, and eccentricity," J. Opt. Soc. Am. A **11,** 1697–1709 (1994).
35. A. Chaparro, C. F. Stromeyer III, R. E. Kronauer, E. Hu, S. Klakadis, and C. Rodgriguez, "Short wave cone input to the red–green detection mechanism," Invest. Ophthalmol. Vis. Res. **36,** S210 (1995).
36. C. F. Stromeyer III, A. Chaparro, A. Tolias, and R. E. Kronauer, "Equiluminant settings change markedly with temporal frequency," Invest. Ophthalmol. Vis. Sci. **36,** S210 (1995).
37. C. F. Stromeyer III, R. E. Kronauer, A. Ryu, A. Chaparro, and R. T. Eskew, Jr., "Contributions of human long-wave and middle wave cones to motion detection," J. Physiol. **485,** 221–243 (1995).
38. L. T. Maloney, "The slopes of the psychometric function at different wavelengths," Vision Res. **30,** 129–136 (1990).
39. C. F. Stromeyer, J. Lee, and R. T. Eskew, Jr., "Peripheral chromatic sensitivity for flashes: a post-receptoral red–green asymmetry," Vision Res. **32,** 1865–1873 (1992).